
Fully Sparse 3D Object Detection

Lue Fan
CASIA

Feng Wang
TuSimple

Naiyan Wang
TuSimple

Zhaoxiang Zhang
CASIA

{fanlue2019, zhaoxiang.zhang}@ia.ac.cn {feng.wff, winsty}@gmail.com

Abstract

As the perception range of LiDAR increases, LiDAR-based 3D object detection becomes a dominant task in the long-range perception task of autonomous driving. The mainstream 3D object detectors usually build dense feature maps in the network backbone and prediction head. However, the computational and spatial costs on the dense feature map are quadratic to the perception range, which makes them hardly scale up to the long-range setting. To enable efficient long-range LiDAR-based object detection, we build a fully sparse 3D object detector (FSD). The computational and spatial cost of FSD is roughly linear to the number of points and independent of the perception range. FSD is built upon the general sparse voxel encoder and a novel sparse instance recognition (SIR) module. SIR first groups the points into instances and then applies instance-wise feature extraction and prediction. In this way, SIR resolves the issue of center feature missing, which hinders the design of the fully sparse architecture for all center-based or anchor-based detectors. Moreover, SIR avoids the time-consuming neighbor queries in previous point-based methods by grouping points into instances. We conduct extensive experiments on the large-scale Waymo Open Dataset to reveal the working mechanism of FSD, and state-of-the-art performance is reported. To demonstrate the superiority of FSD in long-range detection, we also conduct experiments on Argoverse 2 Dataset, which has a much larger perception range (200m) than Waymo Open Dataset (75m). On such a large perception range, FSD achieves state-of-the-art performance and is $2.4\times$ faster than the dense counterpart. Our code is released at <https://github.com/TuSimple/SST>.

1 Introduction

Autonomous driving systems are eager for efficient long-range perception for downstream tasks, especially in high-speed scenarios. Current 3D LiDAR-based object detectors usually convert sparse features into dense feature maps for further feature extraction and prediction. For simplicity, we name the detectors utilizing dense feature maps as **dense detectors**. Dense detectors perform well on current popular benchmarks [31, 7, 2], where the perception range is relatively short (less than 75 meters). However, it is impractical to scale the dense detectors to the long-range setting (more than 200 meters, Fig. 2). In such settings, the computational and spatial complexity on dense feature maps is quadratic to the perception range. Fortunately, the sparsity of LiDAR point clouds also increases as the perception range extends (see Fig. 2), and the calculation on the

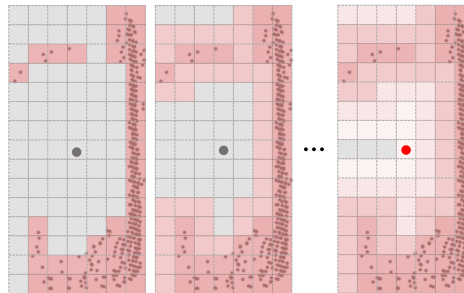


Figure 1: Illustration of **center feature missing** and **feature diffusion** on dense feature maps from Bird's Eye View. The empty instance center (red dot) is filled by the features diffused from occupied voxels (with LiDAR points), after several convolutions.

unoccupied area is essentially unnecessary. Given the inherent sparsity, an essential solution for efficient long-range detection is to remove the dense feature maps and make the network architectures *fully sparse*.

However, removing the dense feature map is non-trivial since it plays a critical role in current designs. Commonly adopted sparse voxel encoders [38, 5, 29] only extract the features on the non-empty voxels for efficiency. So without dense feature maps, the object centers are usually empty, especially for large objects. We name this issue as “**Center Feature Missing (CFM)**” (Fig. 1). Almost all popular voxel or pillar based detectors [28, 5, 42, 30, 38] in this field adopt center-based or anchor-based assignment since the center feature is the best representation of the whole object. However, CFM significantly weakens the representation power of the center voxels, even makes the center feature empty in some extreme cases like super large vehicles. Given this difficulty, many previous detectors [38, 42, 28, 5] have to convert sparse voxels to dense feature maps in Bird’s Eye View after the sparse voxel encoder. Then they resolve the CFM issue by applying convolutions on the dense feature maps to diffuse features to instance centers, which we name as **feature diffusion** (Fig. 1).

To properly remove the dense feature map, we then investigate the purely point-based detectors because they are naturally fully sparse. However, two drawbacks limit the usage of point-based methods in the autonomous driving scenario. (1) Inefficiency: The time-consuming neighborhood query [24] is the long-standing difficulty to apply it to large-scale point cloud (more than 100K points). (2) Coarse representation: To reduce the computational overhead, point-based methods aggressively downsample the whole scene to a fixed number of points. The aggressive downsampling leads to inevitable information loss and insufficient recall of foreground objects [40, 43]. As a result, very few purely point-based detectors have reached state-of-the-art performance in the recent benchmarks with large-scale point clouds.

In this paper, we propose **Fully Sparse Detector (FSD)**, which takes the advantages of both sparse voxel encoder and point-based instance predictor. Since the central region might be empty, the detector has to predict boxes from other non-empty parts of instances. However, predicting the whole box from individual parts causes a large variance on the regression targets, making the results noisy and inconsistent. This motivates us to first group the points into an instance, then we further extract the instance-level feature and predict a single bounding box from the instance feature. To implement this principle, FSD first utilizes the sparse voxel encoder [38, 29, 5] to extract voxel features, then votes object centers based on these features as in VoteNet [23]. Then the *Instance Point Grouping (IPG)* module groups the voted centers into instances via Connected Components Labeling. After grouping, a point-based *Sparse Instance Recognition (SIR)* module extracts instance features and predicts the whole bounding boxes. As a point-based module, SIR has several desired properties. (1) Unlike previous point-based modules, SIR treats instances as groups, and does not apply the time-consuming neighborhood query for further grouping. (2) Similar to dynamic voxelization [46], SIR leverages *dynamic broadcast/pooling* for tensor manipulation to avoid point sampling or padding. (3) Since SIR covers the whole instance, it builds a sufficient receptive field regardless of the physical size of the instance. We list our contributions as follows.

- We propose the concept of Fully Sparse Detector (FSD), which is the essential solution for efficient long-range LiDAR detection. We further propose Sparse Instance Recognition (SIR) to overcome the issue of Center Feature Missing in sparse feature maps. Combining SIR with general sparse voxel encoders, we build an efficient and effective FSD implementation.
- FSD achieves state-of-the-art performance on the commonly used Waymo Open Dataset. Besides, we further apply our method to the recently released Argoverse 2 dataset to demonstrate the superiority of FSD in long-range detection. Given its challenging 200 meters perception range, FSD showcases state-of-the-art performance while being $2.4\times$ faster than state-of-the-art dense detectors.

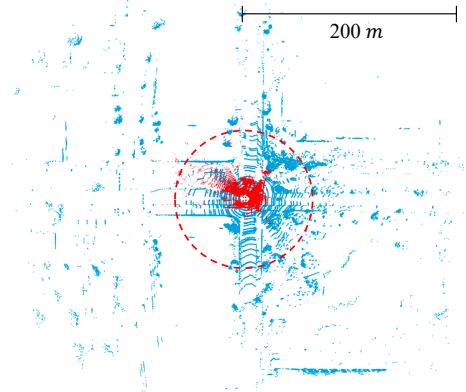


Figure 2: Short-range point clouds (red, from KITTI [7]) v.s. long-range point clouds (blue, from Argoverse 2 [37]). The radius of the red circle is 75 meters. The sparsity quickly increases as the range extends.

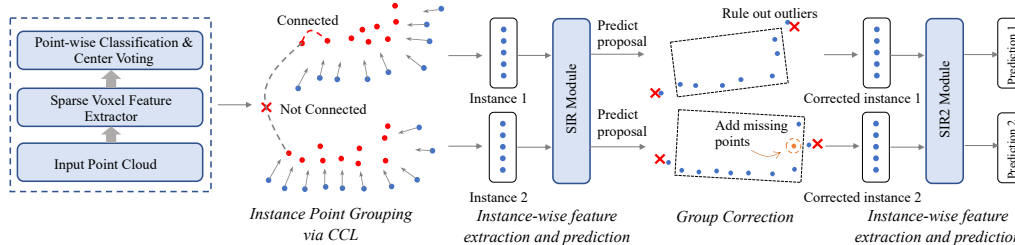


Figure 3: Overall architecture of FSD. For simplicity, we only use two instances to illustrate the pipeline. Red dots are the voted centers from each LiDAR point (blue dots). The SIR module and the SIR2 module all contain 3 SIR layers.

2 Related Work

Voxel-based dense detectors Pioneering work VoxelNet [45] uses dense convolution for voxel feature extraction. Although it achieves competitive performance, it is inefficient to apply dense convolution to 3D voxel representation. PIXOR [39] and PointPillars [13] adopt 2D dense convolution in Bird’s Eye View (BEV) feature map achieving significant efficiency improvement. We name such detectors as **dense detectors** since they convert the sparse point cloud into dense feature maps.

Voxel-based semi-dense detectors Different from the dense detectors, **semi-dense detectors** incorporate both sparse features and dense features. SECOND [38] adopts sparse convolution to extract the sparse voxel features in 3D space, which then are converted to dense feature maps in BEV to enlarge the receptive field and integrate with 2D detection head [19, 25, 44]. Based on SECOND-style semi-dense detectors, many methods attach a second stage for fine-grained feature extraction and proposal refinement [29, 28, 30, 3]. It is noteworthy that the semi-dense detector is hard to be trivially lifted to the fully sparse detector since it will face the issue of Center Feature Missing, as we discussed in Sec. 1.

Point-based sparse detectors The purely point-based detectors are born to be fully sparse. PointRCNN [27] is the pioneering work to build the purely point-based detector. 3DSSD [40] accelerates the point-based method by removing the feature propagation layer and refinement module. VoteNet [23] first makes a center voting and then generates proposals from the voted center achieving better precision. Albeit many methods have tried to accelerate the point-based method, the time-consuming neighborhood query is still unaffordable in large-scale point clouds (more than 100k points per scene). So current benchmarks [31, 2] with large-scale point clouds are dominated by voxel-based dense/semi-dense detectors [11, 30, 15].

3 Methodology

3.1 Overall Architecture

Following the motivation of instances as groups, we have four steps to build the fully sparse detector (FSD): 1) We first utilize a sparse voxel encoder [5, 29, 38] to extract voxel features and vote object centers (Sec. 3.2). 2) Instance Point Grouping groups foreground points into instances based on the voting results (Sec. 3.2). 3) Given the grouping results, Sparse Instance Recognition (SIR) module extracts instance/point features and generates proposals (Sec. 3.3). 4) The proposals are utilized to correct the point grouping and refine the proposals via another SIR module (Sec. 3.4).

3.2 Instance Point Grouping

Classification and Voting We first extract voxel features from the point cloud with a sparse voxel encoder. Although FSD is not restricted to a certain sparse voxel encoder, we utilize sparse attention block in SST [5] due to its demonstrated effectiveness. Then we build point features by concatenating voxel features and the offsets from points to their corresponding voxel centers. These point features are passed into two heads for foreground classification and center voting. The voting is similar to VoteNet [23], where the model predicts the offsets from foreground points to corresponding object

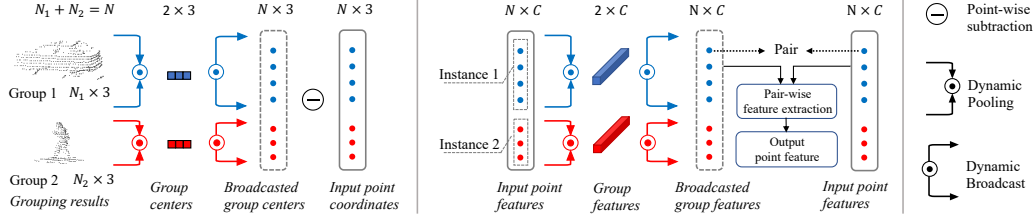


Figure 4: Illustration of building instance-level point operators with dynamic broadcast/pooling. Best viewed in color. Left: calculating center-to-neighbor offsets given raw point clouds. Right: updating point features. Note that the operation is parallel among all instances.

centers. L1 loss [25] and Focal Loss [18] are adopted as voting loss L_{vote} and semantic classification loss L_{sem} .

Connected Components Labeling (CCL) To group points into instances, we regard all the predicted centers (red dots in Fig. 3) as vertices in a graph. Two vertices are connected if their distance is smaller than a certain threshold. Then a connected component in this graph can be viewed as an instance, and all points voted to this connected component share a group ID. Unlike the ball query in VoteNet, our CCL-based grouping greatly avoids fragmented instances. Although there are many elaborately designed instance grouping methods [12, 34, 10], we opt for the simple CCL because it is adequate in our design and can be implemented by the efficient depth-first search.

3.3 Sparse Instance Recognition

3.3.1 Preliminaries: Dynamic Broadcast/Pooling

Given N points belong to M groups, we define their corresponding group ID array as I in shape of $[N,]$ and their feature array as F in shape of $[N, C]$, where C is the feature dimensions. $F^{(i)}$ is the feature array of points belonging to the i -th group. Dynamic pooling aggregates each $F^{(i)}$ into one group feature g_i of shape $[C,]$. Thus we have $g_i = p(F^{(i)})$, where p is a symmetrical pooling function. The dynamic pooling on all group features G of shape $[M, C]$ is formulated as $G = p(F, I)$. The dynamic broadcast can be viewed as the inverse operation to dynamic pooling, which broadcasts g_i to all the points in the i -th group. Since the broadcasting is essentially an indexing operation, we use the indexing notation $[]$ to denote it as $G[I]$, which is in shape of $[N, C]$. Dynamic broadcast/pooling is very efficient because it can be implemented with high parallelism on modern devices and well fits the sparse data with dynamic size.

The prerequisite of dynamic broadcast/pooling is that each point *uniquely* belongs to a group. In other words, groups should not overlap with each other. Thanks to the motivation of instances as groups, the groups in 3D space do not overlap with each other naturally.

3.3.2 Formulation of Sparse Instance Recognition

After grouping points into instances in Sec. 3.2, we can directly extract instance features by some basic point-based networks like PointNet, DGCNN, etc. There are three elements to define a basic point-based module: *group center*, *pair-wise feature* and *group feature aggregation*.

Group center The group center is the representative point of a group. For example, in the ball query, it is the local origin of the sphere. In SIR, the group center is defined as the centroid of all voted centers in a group.

Pair-wise feature defines the input for per point feature extraction. SIR adopts two kinds of features: 1) relative coordinate between group center and each point, 2) feature concatenation between group and each neighbor point. Taking feature concatenation as example and using the notations in 3.3.1, the pair-wise feature can be denoted as $CAT(F, G[I])$, where CAT is channel concatenation.

Group feature aggregation In a group, a pooling function is used to aggregate neighbor features. SIR applies dynamic pooling to aggregate feature array F . Following the notations in 3.3.1, we have $G = p(F, I)$, where G is the aggregated group features.

Integration Combining the three basic elements, we could build many variants of point-based operators, such as PointNet [22], DGCNN [35], Meta-Kernel [4], etc. Fig. 4 illustrates the basic idea of how to build an instance-level point operator with dynamic broadcast/pooling. In our design, we adopt the formulation of VFE [45] as the basic structure of SIR layers, which is basically a two-layer PointNet. In the l -th layer of SIR module, given the input point-wise feature array F_l , point coordinates array X , the voted center X' and group ID array I , the output of l -th layer can be formulated as:

$$F'_l = \text{LinNormAct}(\text{CAT}(F_l, X - p_{\text{avg}}(X', I)[I])), \quad (1)$$

$$F_{l+1} = \text{LinNormAct}(\text{CAT}(F'_l, p_{\text{max}}(F'_l, I)[I])), \quad (2)$$

where LinNormAct is a fully-connected layer followed by a normalization layer [33] and an activation function [9]. The p_{avg} and the p_{max} are average-pooling and max-pooling function, respectively. The output F_{l+1} can be further used as the input of the next SIR layer, so our SIR module is a stack of a couple of basic SIR layers.

3.3.3 Sparse Prediction

With the formulation in Eqn. 1 and Eqn. 2, SIR extracts features of all instances dynamically in parallel. And then SIR makes **sparse prediction** for all groups. In contrast to two-stage sparse prediction, our proposals (i.e., groups) do not overlap with each other. Unlike one-stage dense prediction, we only generate a single prediction for a group. Sparse prediction avoids the difficulty of label assignment in dense prediction when the center feature is missing, because there is no need to attach anchors or anchor points to non-empty voxels. It is noteworthy that the fully sparse architecture may face a severe imbalance problem: short-range objects contain much more points than long-range objects. Some methods [1, 4] use hand-crafted normalization factors to mitigate the imbalance. Instead, SIR avoids the imbalance because it only generates a single prediction for a group regardless of the number of points in the group.

Specifically, for each SIR layer, there is a $G_l = p_{\text{max}}(F'_l, I)$ in Eqn. 2, which can be viewed as the group features. We concatenate all G_l from each SIR layer in channel dimension and use the concatenated group features to predict bounding boxes and class labels via MLPs. All the groups whose centers fall into ground-truth boxes are positive samples. For positive samples, the regression branch predicts the offsets from group centers to ground-truth centers and object sizes and orientations. L1 loss [25] and Focal Loss [18] are adopted as regression loss L_{reg} and classification loss L_{cls} , respectively.

3.4 Group Correction

There is inevitable incorrect grouping in the Instance Point Grouping module. For example, some foreground points may be missed, or some groups may be contaminated by background clutter. So we leverage the bounding box proposals from SIR to correct the grouping. The points inside a proposal belong to a corrected group regardless of their previous group IDs. After correction, we apply an additional SIR to these new groups. To distinguish it from the first SIR module, we denote the additional SIR module as SIR2.

SIR2 predicts box residual from the proposal to its corresponding ground-truth box, following many two-stage detectors. To make SIR2 aware of the size and location of a proposal, we adopt the offsets from inside points to proposal boundaries as extra point features following [16]. The regression loss is denoted as $L_{\text{res}} = L1(\Delta_{\text{res}}, \widehat{\Delta}_{\text{res}})$, where Δ_{res} is the ground-truth residual and $\widehat{\Delta}_{\text{res}}$ is the predicted residual. Following previous methods [29, 28], the 3D Intersection over Union (IoU) between the proposal and ground-truth serves as the soft classification label in SIR2. Specifically, the soft label q is defined as $q = \min(1, \max(0, 2IoU - 0.5))$, where IoU is the IoU between proposals and corresponding ground-truth. Then cross entropy loss is adopted to train the classification branch, denoted as L_{iou} . Taking all the loss functions in grouping (Sec. 3.2) and sparse prediction into account, we have

$$L_{\text{total}} = L_{\text{sem}} + L_{\text{vote}} + L_{\text{reg}} + L_{\text{cls}} + L_{\text{res}} + L_{\text{iou}}, \quad (3)$$

where we omit the normalization factors for simplicity.

3.5 Discussion

The center voting in FSD is inspired by VoteNet [23], while FSD has two essential differences from VoteNet.

- After voting, VoteNet simply aggregates features around the voted centers without further feature extraction. Instead, FSD builds a highly efficient SIR module taking advantage of dynamic broadcast/pooling for further instance-level feature extraction. Thus, FSD extracts more powerful instance features, which is experimentally demonstrated in Sec. 4.6.
- VoteNet is a typical point-based method. As we discussed in Sec. 1, it aggressively down-samples the whole scene to a fixed number of points for efficiency, causing inevitable information loss. Instead, the dynamic characteristic and efficiency of SIR enable fine-grained point feature extraction from any number of input points without any downsampling. In Sec. 4.6, we showcase the efficiency of our design in processing large-scale point clouds and the benefits from fine-grained point representation.

4 Experiments

4.1 Setup

Dataset: Waymo Open Dataset (WOD) We conduct our main experiments on WOD [31]. WOD is currently the largest and most trustworthy benchmark for LiDAR-based 3D object detection. WOD contains 1150 sequences (more than 200K frames), 798 for training, 202 for validation, and 150 for test. The detection range in WOD is 75 meters (cover area of $150m \times 150m$).

Dataset: Argoverse 2 (AV2) We further conduct long-range experiments on the recently released Argoverse 2 dataset [37] to demonstrate the superiority of FSD in long-range detection. AV2 has a similar scale to WOD, and it contains 1000 sequences in total, 700 for training, 150 for validation, and 150 for test. In addition to *average precision* (AP), AV2 adopts a *composite score* as evaluation metric, which takes both AP and localization errors into account. The perception range in AV2 is 200 meters (cover area of $400m \times 400m$), which is much larger than WOD. Such a large perception range leads to a huge memory footprint for dense detectors.

Model Variants To demonstrate the generality of SIR, we build two FSD variants. FSD_{sst} adopts the emerging single stride sparse transformer [5] as sparse voxel feature extractor. FSD_{spconv} is built upon sparse convolution based U-Net in PartA2 [29]. Unless otherwise specified, we use FSD_{sst} in the experiments.

Implementation Details We use 4 sparse regional attention blocks [5] in SST as our voxel feature extractor. The SIR module and SIR2 module consist of 3 and 6 SIR layers, respectively. A SIR layer is defined by Eqn. 1 and Eqn. 2. Our SST-based model converges much faster than SST, so we train our models for 6 epochs instead of the $2 \times$ schedule (24 epochs) in SST. For FSD_{spconv} , in addition to the 6-epoch schedule, we adopt a longer schedule (12 epochs) for better performance. Different from the default setting in MMDetection3D, we decrease the number of pasted instances in the CopyPaste augmentation, to prevent FSD from overfitting.

4.2 Comparison to State-of-the-art Methods

We first compare FSD with state-of-the-art detectors and our baseline in Table 1. FSD achieves the state-of-the-art performance among all the mainstream detectors. Thanks to the fine-grained feature extraction in SIR, FSD also obtains exciting performance on *Pedestrian* class and *Cyclist* class with single-frame point clouds.

4.3 Study of Treatments to Center Feature Missing

In what follows, we conduct experiments on WOD to elaborate the issue of **Center Feature Missing (CFM)**. We first build several models with different characteristics. Note that all the following models adopt the same voxelization resolution, so they face the same degree of CFM at the beginning.

- FSD_{plain} : After the sparse voxel encoder, FSD_{plain} directly predicts the box from each voxel. The voxels inside ground-truth boxes are assigned *positive*. Although FSD_{plain} uses the most

Table 1: Performances on the Waymo Open Dataset validation split. All models only take single-frame point cloud as input without any test-time augmentations or model ensemble. All classes are trained in a single model in FSD. Different from the default CopyPaste in MMDetection3D, we decrease the number of pasted instances to prevent overfitting. †: Longer schedule (12 epochs).

Methods	mAP/mAPH L2	Vehicle 3D AP/APH		Pedestrian 3D AP/APH		Cyclist 3D AP/APH	
		L1	L2	L1	L2	L1	L2
SECOND [38]	61.0/57.2	72.3/71.7	63.9/63.3	68.7/58.2	60.7/51.3	60.6/59.3	58.3/57.0
MVF [46]	-/-	62.9/-	-/-	65.3/-	-/-	-/-	-/-
AFDet [6]	-/-	63.7/-	-/-	-/-	-/-	-/-	-/-
Pillar-OD [36]	-/-	69.8/-	-/-	72.5/-	-/-	-/-	-/-
RangeDet [4]	65.0/63.2	72.9/72.3	64.0/63.6	75.9/71.9	67.6/63.9	65.7/64.4	63.3/62.1
PointPillars [13]	62.8/57.8	72.1/71.5	63.6/63.1	70.6/56.7	62.8/50.3	64.4/62.3	61.9/59.9
Voxel RCNN [3]	-/-	75.6/-	66.6/-	-/-	-/-	-/-	-/-
RCD [1]	-/-	69.0/68.5	-/-	-/-	-/-	-/-	-/-
VoTr-TSD [21]	-/-	74.9/74.3	65.9/65.3	-/-	-/-	-/-	-/-
LiDAR-RCNN [16]	65.8/61.3	76.0/75.5	68.3/67.9	71.2/58.7	63.1/51.7	68.6/66.9	66.1/64.4
Pyramid RCNN [20]	-/-	76.3/75.7	67.2/66.7	-/-	-/-	-/-	-/-
Voxel-to-Point [14]	-/-	77.2/-	69.8/-	-/-	-/-	-/-	-/-
3D-MAN [41]	-/-	74.5/74.0	67.6/67.1	71.7/67.7	62.6/59.0	-/-	-/-
M3DETR [8]	61.8/58.7	75.7/75.1	66.6/66.0	65.0/56.4	56.0/48.4	65.4/64.2	62.7/61.5
Part-A2-Net [29]	66.9/63.8	77.1/76.5	68.5/68.0	75.2/66.9	66.2/58.6	68.6/67.4	66.1/64.9
CenterPoint-Pillar [42]	-/-	76.1/75.5	68.0/67.5	76.1/65.1	68.1/57.9	-/-	-/-
CenterPoint-Voxel [42]	69.8/67.6	76.6/76.0	68.9/68.4	79.0/73.4	71.0/65.8	72.1/71.0	69.5/68.5
IA-SSD [43]	62.3/58.1	70.5/69.7	61.6/61.0	69.4/58.5	60.3/50.7	67.7/65.3	65.0/62.7
PV-RCNN [28]	66.8/63.3	77.5/76.9	69.0/68.4	75.0/65.6	66.0/57.6	67.8/66.4	65.4/64.0
RSN [32]	-/-	75.1/74.6	66.0/65.5	77.8/72.7	68.3/63.7	-/-	-/-
SST_TS [5]	-/-	76.2/75.8	68.0/67.6	81.4/74.0	72.8/65.9	-/-	-/-
SST [5]	67.8/64.6	74.2/73.8	65.5/65.1	78.7/69.6	70.0/61.7	70.7/69.6	68.0/66.9
AFDetV2 [11]	71.0/68.8	77.6/77.1	69.7/69.2	80.2/74.6	72.2/67.0	73.7/72.7	71.0/70.1
PillarNet-34 [26]	71.0/68.5	79.1/78.6	70.9/70.5	80.6/74.0	72.3/66.2	72.3/71.2	69.7/68.7
PV-RCNN++ [30]	68.4/64.9	78.8/78.2	70.3/69.7	76.7/67.2	68.5/59.7	69.0/67.6	66.5/65.2
PV-RCNN++(center) [30]	71.7/69.5	79.3/78.8	70.6/70.2	81.3/76.3	73.2/68.0	73.7/72.7	71.2/70.2
FSD _{spconv} (ours)	71.9/69.7	77.8/77.3	68.9/68.5	81.9/76.4	73.2/68.0	76.5/75.2	73.8/72.5
FSD _{ast} (ours)	71.5/69.2	76.8/76.3	67.9/67.5	81.3/75.3	72.5/67.0	77.2/76.0	74.4/73.2
FSD _{spconv} (ours) †	72.9/70.8	79.2/78.8	70.5/70.1	82.6/77.3	73.9/69.1	77.1/76.0	74.4/73.3

straightforward solution for CFM, it suffers from the large variance of regression targets and low-quality predictions from hard voxels.

- **SST_{center}**: It replaces the anchor-based head in SST with CenterHead [44, 42]. Based on sparse voxel encoder, SST_{center} converts sparse voxels into dense feature maps and applies several convolutions to diffuse features to the empty object centers as in Fig. 1. Then it makes predictions from the diffused center feature.
- **FSD_{nogc}**: It removes the group correction and SIR2 module in FSD.
- **CenterPoint-PP**: It does not resort to any sparse voxel encoders. Instead, it applies multiple dense convolutions soon after voxelization for feature diffusion, greatly eliminating CFM. It also is equipped with CenterHead avoiding large variance of regression targets.

Experiments and analyses

There is usually a quite large unoccupied area around the centers of large vehicles. Thus the performance of large vehicles is an appropriate indicator that reveals the effect of CFM. So we build a customized evaluation tool, which breaks down the object length following the COCO evaluation [17]. Then we use it to evaluate the performance of vehicles with different lengths. Table 2 shows the results, and we list our findings as follows.

Table 2: Vehicle detection with vehicle length breakdown. †: re-implemented ourselves. *: official Waymo L2 overall metric. Arrows indicate the performance changes from SST_{center}.

Methods	Vehicle length (m)				Official*
	[0, 4)	[4, 8)	[8, 12)	[12, +∞)	
CenterPoint-PP†	34.3	69.3	42.0	43.6	66.2
FSD _{plain}	32.2	64.6	41.3	42.2	62.3
SST _{center} [5]	36.0	69.4	33.7	30.5	66.3
FSD _{nogc}	33.5 ↓ 2.5	68.2 ↓ 1.2	47.7 ↑ 14.0	47.9 ↑ 17.4	65.2 ↓ 1.1
FSD	36.7 ↑ 0.7	71.0 ↑ 1.6	51.3 ↑ 17.6	53.7 ↑ 23.2	69.3 ↑ 3.0

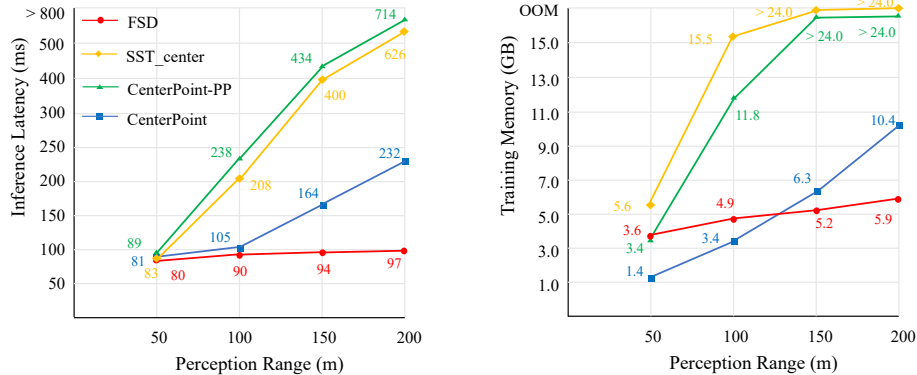


Figure 5: **Memory footprints and inference latency in different perception ranges.** We use FSD_{sst} (Sec. 4.1) here. Statistics are obtained on a single 3090 GPU with batch size 1. Inference latency is evaluated by the standard benchmark script in MMDetection3D without any test-time optimization. CenterPoint-PP and SST_{center} are defined in Sec. 4.3. Best viewed in color.

- Comparing FSD_{plain} with SST_{center} , they share the same attention-based sparse voxel encoder. However, the trend is totally opposite w.r.t vehicle size. With feature diffusion, SST_{center} attains much worse performance than FSD_{plain} on large vehicles. It suggests feature diffusion is a sub-optimal solution for CFM in the case of large objects. For those large objects, the features may not be diffused to the centers or the diffused features are too weak to make accurate predictions.
- However, FSD_{plain} obtains the worst performance among all detectors on vehicles with normal sizes. Note that the CFM issue is minor for the normal size vehicles. So, in this case, the center-based assignment in SST_{center} shows its superiority to the assignment in FSD_{plain} . It suggests the solution for CFM in FSD_{plain} is also sub-optimal, even if it achieves better performance in large objects.
- Comparing FSD_{nogc} with SST_{center} , they share the same sparse voxel encoder while FSD_{nogc} replaces the dense part in SST_{center} with SIR. The huge improvements of FSD_{nogc} on large vehicles fairly reveal that SIR effectively resolves CFM and is better than feature diffusion.
- CenterPoint-PP suffers much less from CFM because it leverages dense feature maps from very beginning of the network. It is also equipped with the advanced center-based assignment. Even so, FSD_{nogc} and FSD still outperform CenterPoint-PP, especially on large vehicles.

Table 3: Performance in Argoverse 2 validation split. †: provided by authors of AV2 dataset. ‡: Weak CopyPaste augmentation for preventing overfitting (one instance per class). *: re-implemented by ourselves. C-Barrel: construction barrel. MPC-Sign: mobile pedestrian crossing sign. A-Bus: articulated bus. C-Cone: construction cone. V-Trailer: vehicular trailer. We omit the results of dog, wheelchair and message board trailer because these categories contain very few instances. The average results take all categories into account, including the omitted categories. We mark the categories attaining notable improvements in **bold**.

Methods	Average	Vehicle	Bus	Pedestrian	Stop Sign	Box Truck	Bollard	C-Barrel	Motorcyclist	MPC-Sign	Motorcycle	Bicycle	A-Bus	School Bus	Truck Cab	C-Cone	V-Trailer	Sign	Large Vehicle	Stroller	Bicyclist
<i>Precision</i>																					
CenterPoint† [42]	13.5	61.0	36.0	33.0	28.0	26.0	25.0	22.5	16.0	16.0	12.5	9.5	8.5	7.5	8.0	8.0	7.0	6.5	3.0	2.0	14
CenterPoint*	22.0	67.6	38.9	46.5	16.9	37.4	40.1	32.2	28.6	27.4	33.4	24.5	8.7	25.8	22.6	29.5	22.4	6.3	3.9	0.5	20.1
FSD	24.0	67.1	39.8	57.4	21.3	38.3	38.3	38.1	30.0	23.6	38.1	25.5	15.6	30.0	20.1	38.9	23.9	7.9	5.1	5.7	27.0
FSD _{sponv} ‡	28.2	68.1	40.9	59.0	29.0	38.5	41.8	42.6	39.7	26.2	49.0	38.6	20.4	30.5	14.8	41.2	26.9	11.9	5.9	13.8	33.4
<i>Composite Score</i>																					
CenterPoint*	17.6	57.2	32.0	35.7	13.2	31.0	28.9	25.6	22.2	19.1	28.2	19.6	6.8	22.5	17.4	22.4	17.2	4.8	3.0	0.4	16.7
FSD	19.1	56.0	33.0	45.7	16.7	31.6	27.7	30.4	23.8	16.4	31.9	20.5	12.0	25.6	15.9	29.2	18.1	6.4	3.8	4.5	22.1
FSD _{sponv} ‡	22.7	57.7	34.2	47.5	23.4	31.7	30.9	34.4	32.3	18.0	41.4	32.0	15.9	26.1	11.0	30.7	20.5	9.5	4.4	11.5	28.0

4.4 Long-range Detection

Several widely adopted 3D detection benchmarks [31, 7, 2] have relatively short perception range. To unleash the potential of FSD, we conduct long-range detection experiments on the recently released

Argoverse 2 dataset (AV2), with a perception range of 200 meters. In addition, AV2 contains objects in 30 classes, facing the challenging long-tail issue.

Main results We first list the main results of FSD on AV2 in Table 3. The authors of AV2 provide a baseline CenterPoint model, but the results are mediocre. To make a fair comparison, we re-implement a stronger CenterPoint model on the AV2 dataset. The re-implemented CenterPoint adopts the same training scheme with FSD, including ground-truth sampling to alleviate the long-tail issue. FSD outperforms CenterPoint in the average metric. It is noteworthy that FSD significantly outperforms CenterPoint in some tiny objects (e.g., Pedestrian, Construction Cone) as well as some objects with extremely large sizes (e.g., Articulated Bus, School Bus). We owe this to the virtue of instance-level fine-grained feature extraction in SIR.

Range Scaling To demonstrate the efficiency of FSD in long-range detection, we depict the trend of training memory and inference latency of three detectors when the perception range increases in Fig. 5. Fig. 5 shows dramatic latency/memory increase when applying dense detectors to larger perception ranges. Designed to be fully sparse, the resource needed for FSD is roughly linear to the number of input points, so its memory and latency only slightly increase as the perception range extends.

4.5 More Sparse Scenes

Argoverse 2 dataset provides a highly reliable HD map, which could be utilized as a prior to remove uninterested regions making the scene more sparse. Thus we proceed with experiments removing some uninterested regions to show the advantages of FSD in more sparse scenarios. The results are summarized in Table 4. FSD has a significantly lower memory footprint and latency with an acceptable precision loss after removing the uninterested regions. On the contrary, the efficiency improvement of CenterPoint is minor. It reveals that FSD benefits more from the increase of data sparsity, which is another advantage of the fully sparse architecture.

Table 4: Performance with different detection areas. †: Region of Interest is defined by the HD map in AV2 dataset.

	Mem.	FSD Latency(ms)	mAP	Mem.	CenterPoint Latency(ms)	mAP
all	5.9	97	24.0	10.4	232	22.0
only RoI†	3.2 ↓ 45.8%	81 ↓ 16.5%	23.2	9.9 ↓ 4.8%	227 ↓ 2.2%	21.5
w/o ground	2.3 ↓ 61.0%	74 ↓ 25.8%	21.0	9.7 ↓ 6.7%	217 ↓ 6.4%	19.8

4.6 Ablation Study

Effectiveness of Components In addition to FSD_{plain} and FSD_{nogc} (Sec. 4.3), we also degrade FSD to FSD_{agg} to understand the mechanism of FSD. In FSD_{agg} , we aggregate grouped point features by dynamic pooling and then directly make predictions from the pooled features, after Instance Point Grouping. FSD_{agg} is similar to the way in VoteNet [23] as we discussed in Sec. 3.5. Thus, FSD_{agg} can explicitly leverage instance-level features other than the point-level features in FSD_{plain} . However, FSD_{agg} can not take advantage of further point feature extraction in SIR. As can be seen in Table 5, the improvement is limited if we only apply grouping without SIR. The combination of grouping and SIR attain notable improvements.

Table 5: Ablation of design factors in SIR. Performances are evaluated on Waymo validation split.

	Grouping	SIR	Group Correction	Vehicle	L2 3D APH Pedestrian	Cyclist
FSD_{plain}				62.29	64.31	64.49
FSD_{agg}	✓			63.13	65.13	64.52
FSD_{nogc}	✓	✓		65.20	67.39	67.78
FSD	✓	✓	✓	69.30	69.30	69.60

Downsampling in SIR The efficiency of SIR makes it feasible to extract fine-grained point features without any point downsampling. This is another notable difference between FSD and VoteNet. To demonstrate the superiority, we apply voxelization on the raw points before SIR module and treat the centroids of voxels as downsampled points. We conduct experiments on AV2 dataset because it contains a couple of categories in a tiny size, which may be sensitive to downsampling. As expected, small objects have notable performance loss when adopting downsampling, and we list some of them in Table 6. We

Table 6: Performances with different representation granularity. †: Latency of SIR module.

Voxel size	AP				Latency (ms)†
	CC	Bollard	Bicyclist	Stop Sign	
30cm	35.4	36.5	24.6	18.3	3.5
20cm	37.3	37.3	26.4	20.0	4.1
10cm	38.9	38.3	27.0	21.3	4.5
Point	39.3	38.6	27.1	21.5	6.3

also evaluate the inference latency of the SIR module on 3090 GPU. As can be seen, compared with the overall latency (97ms, Fig. 5), the SIR module is highly efficient.

5 Conclusion

This paper proposes FSD, a fully sparse 3D object detector, aiming for efficient long-range object detection. FSD utilizes a highly efficient point-based Sparse Instance Recognition module to solve the center feature missing in fully sparse architecture. FSD achieves not only competitive performance on the widely-used Waymo Open Dataset, but also state-of-the-art performance in the long-range Argoverse 2 dataset with a much faster inference speed than previous detectors.

Limitation A more elaborately designed grouping strategy may help with performance improvements. However, it is beyond our design goal in this paper, and we will pursue it in future work.

References

- [1] Alex Bewley, Pei Sun, Thomas Mensink, Dragomir Anguelov, and Cristian Sminchisescu. Range Conditioned Dilated Convolutions for Scale Invariant 3D Object Detection. *arXiv preprint arXiv:2005.09927*, 2020.
- [2] Holger Caesar, Varun Bankiti, Alex H Lang, Sourabh Vora, Venice Erin Liong, Qiang Xu, Anush Krishnan, Yu Pan, Giancarlo Baldan, and Oscar Beijbom. nuscenes: A multimodal dataset for autonomous driving. In *CVPR*, 2020.
- [3] Jiajun Deng, Shaoshuai Shi, Peiwei Li, Wengang Zhou, Yanyong Zhang, and Houqiang Li. Voxel R-CNN: Towards High Performance Voxel-based 3D Object Detection. In *AAAI*, 2021.
- [4] Lue Fan, Xuan Xiong, Feng Wang, Naiyan Wang, and ZhaoXiang Zhang. RangeDet: In Defense of Range View for LiDAR-Based 3D Object Detection. In *ICCV*, 2021.
- [5] Lue Fan, Ziqi Pang, Tianyuan Zhang, Yu-Xiong Wang, Hang Zhao, Feng Wang, Naiyan Wang, and Zhaoxiang Zhang. Embracing Single Stride 3D Object Detector with Sparse Transformer. In *CVPR*, 2022.
- [6] Runzhou Ge, Zhuangzhuang Ding, Yihan Hu, Yu Wang, Sijia Chen, Li Huang, and Yuan Li. AFDet: Anchor Free One Stage 3D Object Detection. *arXiv preprint arXiv:2006.12671*, 2020.
- [7] Andreas Geiger, Philip Lenz, and Raquel Urtasun. Are we ready for autonomous driving? the kitti vision benchmark suite. In *2012 IEEE conference on computer vision and pattern recognition*. IEEE, 2012.
- [8] Tianrui Guan, Jun Wang, Shiyi Lan, Rohan Chandra, Zuxuan Wu, Larry Davis, and Dinesh Manocha. m3detr: Multi-representation, multi-scale, mutual-relation 3d object detection with transformers.
- [9] Dan Hendrycks and Kevin Gimpel. Gaussian Error Linear Units (GELUs). *arXiv preprint arXiv:1606.08415*, 2016.
- [10] Fangzhou Hong, Hui Zhou, Xinge Zhu, Hongsheng Li, and Ziwei Liu. Lidar-based panoptic segmentation via dynamic shifting network. In *CVPR*, 2021.
- [11] Yihan Hu, Zhuangzhuang Ding, Runzhou Ge, Wenxin Shao, Li Huang, Kun Li, and Qiang Liu. AFDetV2: Rethinking the Necessity of the Second Stage for Object Detection from Point Clouds. *arXiv preprint arXiv:2112.09205*, 2021.
- [12] Li Jiang, Hengshuang Zhao, Shaoshuai Shi, Shu Liu, Chi-Wing Fu, and Jiaya Jia. Pointgroup: Dual-set point grouping for 3d instance segmentation. In *CVPR*, 2020.
- [13] Alex H Lang, Sourabh Vora, Holger Caesar, Lubing Zhou, Jiong Yang, and Oscar Beijbom. PointPillars: Fast Encoders for Object Detection from Point Clouds. In *CVPR*, 2019.
- [14] Jiale Li, Hang Dai, Ling Shao, and Yong Ding. From Voxel to Point: IoU-guided 3D Object Detection for Point Cloud with Voxel-to-Point Decoder. In *ACM-MM*, 2021.
- [15] Yingwei Li, Adams Wei Yu, Tianjian Meng, Ben Caine, Jiquan Ngiam, Daiyi Peng, Junyang Shen, Bo Wu, Yifeng Lu, Denny Zhou, et al. DeepFusion: Lidar-Camera Deep Fusion for Multi-Modal 3D Object Detection. In *CVPR*, 2022.
- [16] Zhichao Li, Feng Wang, and Naiyan Wang. LiDAR R-CNN: An Efficient and Universal 3D Object Detector. In *CVPR*, 2021.

- [17] Tsung-Yi Lin, Michael Maire, Serge Belongie, James Hays, Pietro Perona, Deva Ramanan, Piotr Dollár, and C Lawrence Zitnick. Microsoft COCO: Common Objects in Context. In *European conference on computer vision*. Springer, 2014.
- [18] Tsung-Yi Lin, Priya Goyal, Ross Girshick, Kaiming He, and Piotr Dollár. Focal Loss for Dense Object Detection. In *ICCV*, 2017.
- [19] Wei Liu, Dragomir Anguelov, Dumitru Erhan, Christian Szegedy, Scott Reed, Cheng-Yang Fu, and Alexander C Berg. SSD: Single Shot Multibox Detector. In *ECCV*, 2016.
- [20] Jiageng Mao, Minzhe Niu, Haoyue Bai, Xiaodan Liang, Hang Xu, and Chunjing Xu. Pyramid R-CNN: Towards Better Performance and Adaptability for 3D Object Detection. In *ICCV*, 2021.
- [21] Jiageng Mao, Yujing Xue, Minzhe Niu, Haoyue Bai, Jiashi Feng, Xiaodan Liang, Hang Xu, and Chunjing Xu. Voxel Transformer for 3D Object Detection. In *ICCV*, 2021.
- [22] Charles R Qi, Hao Su, Kaichun Mo, and Leonidas J Guibas. PointNet: Deep Learning on Point Sets for 3D Classification and Segmentation. In *CVPR*, 2017.
- [23] Charles R Qi, Or Litany, Kaiming He, and Leonidas J Guibas. Deep Hough Voting for 3D Object Detection in Point Clouds. In *ICCV*, 2019.
- [24] Charles Ruizhongtai Qi, Li Yi, Hao Su, and Leonidas J Guibas. PointNet++: Deep Hierarchical Feature Learning on Point Sets in a Metric Space. In *NeurIPS*, 2017.
- [25] Shaoqing Ren, Kaiming He, Ross Girshick, and Jian Sun. Faster R-CNN: Towards Real-time Object Detection with Region Proposal Networks. *NeurIPS*, 28, 2015.
- [26] Guangsheng Shi, Ruifeng Li, and Chao Ma. PillarNet: High-Performance Pillar-based 3D Object Detection. *arXiv preprint arXiv:2205.07403*, 2022.
- [27] Shaoshuai Shi, Xiaogang Wang, and Hongsheng Li. PointRCNN: 3D Object Proposal Generation and Detection from Point Cloud. In *CVPR*, 2019.
- [28] Shaoshuai Shi, Chaoxu Guo, Li Jiang, Zhe Wang, Jianping Shi, Xiaogang Wang, and Hongsheng Li. PV-RCNN: Point-Voxel Feature Set Abstraction for 3D Object Detection. In *CVPR*, 2020.
- [29] Shaoshuai Shi, Zhe Wang, Jianping Shi, Xiaogang Wang, and Hongsheng Li. From Points to Parts: 3D Object Detection from Point Cloud with Part-aware and Part-aggregation Network. *IEEE Transactions on Pattern Analysis and Machine Intelligence*, 2020.
- [30] Shaoshuai Shi, Li Jiang, Jiajun Deng, Zhe Wang, Chaoxu Guo, Jianping Shi, Xiaogang Wang, and Hongsheng Li. PV-RCNN++: Point-Voxel Feature Set Abstraction With Local Vector Representation for 3D Object Detection. *arXiv preprint arXiv:2102.00463*, 2021.
- [31] Pei Sun, Henrik Kretzschmar, Xerxes Dotiwalla, Aurelien Chouard, Vijaysai Patnaik, Paul Tsui, James Guo, Yin Zhou, Yuning Chai, Benjamin Caine, et al. Scalability in Perception for Autonomous Driving: Waymo Open Dataset. In *CVPR*, 2020.
- [32] Pei Sun, Weiyue Wang, Yuning Chai, Gamaleldin Elsayed, Alex Bewley, Xiao Zhang, Cristian Sminchisescu, and Dragomir Anguelov. RSN: Range Sparse Net for Efficient, Accurate LiDAR 3D Object Detection. In *CVPR*, 2021.
- [33] Ashish Vaswani, Noam Shazeer, Niki Parmar, Jakob Uszkoreit, Llion Jones, Aidan N Gomez, Łukasz Kaiser, and Illia Polosukhin. Attention Is All You Need. In *NeurIPS*, 2017.
- [34] Weiyue Wang, Ronald Yu, Qiangui Huang, and Ulrich Neumann. SGPN: Similarity Group Proposal Network for 3d Point Cloud Instance Segmentation. In *CVPR*, 2018.
- [35] Yue Wang, Yongbin Sun, Ziwei Liu, Sanjay E Sarma, Michael M Bronstein, and Justin M Solomon. Dynamic graph cnn for learning on point clouds. *Acm Transactions On Graphics (tog)*, 38(5):1–12, 2019.
- [36] Yue Wang, Alireza Fathi, Abhijit Kundu, David Ross, Caroline Pantofaru, Tom Funkhouser, and Justin Solomon. Pillar-based Object Detection for Autonomous Driving. In *ECCV*, 2020.
- [37] Benjamin Wilson, William Qi, Tanmay Agarwal, John Lambert, Jagjeet Singh, Siddhesh Khandelwal, Bowen Pan, Ratnesh Kumar, Andrew Hartnett, Jhony Kaesemodel Pontes, Deva Ramanan, Peter Carr, and James Hays. Argoverse 2: Next Generation Datasets for Self-Driving Perception and Forecasting. In *NeurIPS Datasets and Benchmarks 2021*, 2021.

- [38] Yan Yan, Yuxing Mao, and Bo Li. SECOND: Sparsely Embedded Convolutional Detection. *Sensors*, 18 (10), 2018.
- [39] Bin Yang, Wenjie Luo, and Raquel Urtasun. PIXOR: Real-time 3D Object Detection from Point Clouds. In *CVPR*, 2018.
- [40] Zetong Yang, Yanan Sun, Shu Liu, and Jiaya Jia. 3DSSD: Point-based 3D Single Stage Object Detector. In *CVPR*, 2020.
- [41] Zetong Yang, Yin Zhou, Zhifeng Chen, and Jiquan Ngiam. 3D-MAN: 3D Multi-Frame Attention Network for Object Detection. In *CVPR*, 2021.
- [42] Tianwei Yin, Xingyi Zhou, and Philipp Krähenbühl. Center-based 3D Object Detection and Tracking. *arXiv preprint arXiv:2006.11275*, 2020.
- [43] Yifan Zhang, Qingyong Hu, Guoquan Xu, Yanxin Ma, Jianwei Wan, and Yulan Guo. Not All Points Are Equal: Learning Highly Efficient Point-based Detectors for 3D LiDAR Point Clouds. In *CVPR*, 2022.
- [44] Xingyi Zhou, Dequan Wang, and Philipp Krähenbühl. Objects as Points. *arXiv preprint arXiv:1904.07850*, 2019.
- [45] Yin Zhou and Oncel Tuzel. VoxelNet: End-to-End Learning for Point Cloud Based 3D Object Detection. In *CVPR*, 2018.
- [46] Yin Zhou, Pei Sun, Yu Zhang, Dragomir Anguelov, Jiyang Gao, Tom Ouyang, James Guo, Jiquan Ngiam, and Vijay Vasudevan. End-to-End Multi-View Fusion for 3D Object Detection in LiDAR Point Clouds. In *CoRL*, 2020.